ISSN 1392-1207. MECHANIKA. Vol. 30, No. 4, 2024: 347–356

Pantograph-Catenary Coupling System Dynamics Analysis with Rigid-Flexible Pantograph for Straddle-Type Monorail

Zhen YANG*, Zixue DU, Zhouzhou XU***, Liang XIN****, Zhongwei HOU*****

*Institute of Urban Rail, Chongqing Jiaotong University, 400074 Chongqing, PR China, E-mail: yangz0000@163.com
**Institute of Urban Rail, Chongqing Jiaotong University, 400074 Chongqing, PR China, E-mail: aaadzx@163.com
***Institute of Urban Rail , Chongqing Jiaotong University, 400074 Chongqing, PR China, E-mail: 33243665@qq.com
****Institute of Urban Rail, Chongqing Jiaotong University, 400074 Chongqing, PR China, E-mail: 984755423@qq.com
*****Institute of Urban Rail, Chongqing Jiaotong University, 400074 Chongqing, PR China, E-mail: 13778257@qq.com

https://doi.org/10.5755/j02.mech.34947

1. Introduction

Public planning authorities often face conflicting demands to provide reliable and accessible high capacity public transportation. In the past, city planners have provided this kind of service by specifying metro systems. However, metro systems are highly costly and involved extensive relocation. In some cases, metro systems are not an option due to existing infrastructure, which results in no high capacity transit system at all. Elevated transit systems avoid the need for costly tunneling and minimize the need to relocate existing utilities; however, elevated metro systems typically require wide visually obtrusive deck construction and often still require extensive destruction of existing infrastructure [1]. Straddle-type monorail, as a new typical form of urban rail transit have some advantages such as: strong climbing capability, small turning radius, less land occupation, low noise, and low manufacturing cost. Those unique technical characteristics have played an important role in urban rail transit [2-4].

The operation practice of Chongqing straddle-type monorail found that the running mechanism of monorail vehicle bogie is different from that of metro bogie and the coupling force of pantograph and catenary is not coordinated, which leads to the problems of current collection slider seriously wear, pantograph structure damage and poor current collection quality. In order to improve pantograph catenary dynamic performance, and ensure the safe and reliable operation of monorail, it has important theoretical significance and application value to study on pantograph-catenary system dynamics of monorail vehicle.

During decades of year's development, the theory of metro pantograph-catenary system dynamics has made great progress. Song Y. et al. [5-7] simplifies the pantograph into several lumped mass objects using the principle of kinetic energy equivalence. But the liner lumped mass model can't reflect the higher frequency vibration of pantograph. Massat et al. [8] establishes three-dimensional rigid body model of pantograph using MSC ADAMS. To determine the dynamic loads in the contact between the pantograph and the wire, Shimanovsky et al. [9] performed the simulation analysis using MSC ADAMS. Ambrosio et al. [10] established a rigid-flexible hybrid model of pantograph. References [11-14] researched the dynamic behaviour of pantograph-catenary system by simplified qualitative analysis and accurate simulation calculation. P. Flores [15-17] representation of the pantograph–catenary interaction by penalty formulations and the unilateral constraints.

The double pantographs-catenary model is established using a FEM (Finite Element Method), and proposed the formula of optimal interval of double pantographs, its validity is verified using the parameters of the European and China high-speed networks [18]. The parameter optimization for pantograph was conducted by Lee based on the results of sensitivity analysis [19]. Benet et al. [20] developed a pantograph simulation program in Visual C which can take into consideration the lateral effect of the wind, the actual arrangement of the cables, the horizontal and the vertical components of the contact force, the horizontal and vertical reactions of the supports and the turning angle of the pantograph head. The influence of the monorail pantograph head parameter on the current collection quality was discussed by a full-scale pantograph model based on the pantograph of Chongqing straddle-type monorail line 3 [21]. The wear of pantograph strip is decreased by optimizing catenary pulling out value of Chongqing straddle-type monorail line 2 [22]. There is no research on pantograph modeling of straddle-type monorail.

Compared with previous researches, the innovation of the present work is that researched the influence of pantograph flexibility on the current collection quality and dynamic behaviour of straddle-type monorail.

2. Rigid-flexible pantograph-catenary coupling system

2.1. Dynamic model of rigid-flexible pantograph

Straddle-type monorail pantograph consists of pantograph base, lower frame, upper frame, supporting rod, steady rod, strip base, pantograph head base, pantograph spring and a damping cylinder (positive pantograph only) and so on (Fig. 1). The coordinate description and constraint relation of flexible body are different from those of rigid body. Floating coordinate system method is the most widely used method the coordinate description of flexible body, which is characterized by the combination of multi-body dynamics and structural dynamics. The floating coordinate method has better calculation efficiency and accuracy for small deformation and low speed and large range motion by using modal technology. This paper, the rigid-flexible coupling model of pantograph is established based on the method of floating coordinate system and virtual body.

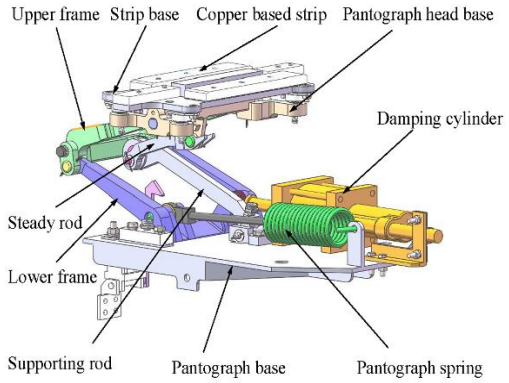

Fig. 1 Pantograph of monorail

The flexible body was divided into l elements by lumped mass finite element method. The moment of inertia of each node was m_k ($k = 1, \cdots, l$). γ_i^k is the Cartesian coordinates of the node k. There is a floating coordinate system attached to the flexible body rigidly (Fig. 2). Eq. (1) is the absolute vector diameter of point k:

$$\gamma_i^k = \gamma_i + A_i\left(\rho_{i0}^k + u_i^k\right), \tag{1}$$

where: γ_i is the absolute vector of the floating coordinate system, A_i is the direction cosine matrix of floating coordinate system relative to absolute coordinate system, ρ_{i0}^k is the vector diameter of point k in the floating coordinate system, u_i^k is the deformation of point k in the floating coordinate system. The deformation of node k is described by translational mode coordinate u_i^k refer Eq. (2):

$$u_i^k = \psi_{di}^k w_i^k, \tag{2}$$

where: ψ_{di}^k is translational modal vector matrix, w_i^k is modal coordinate matrix.

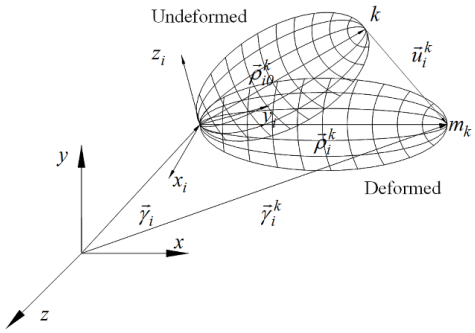

Fig. 2 Description of flexible body coordinate system

Integration flexible body on virtual body, the dynamic equation of flexible system is obtained refer to Eq. (3). Only flexible body has stiffness, so the stiffness matrix is 0 except for the corresponding term of modal coordinates of flexible body. The dynamic equation of flexible system in differential algebraic form is obtained by eliminating the generalized coordinate term of virtual body. The dynamic equations of flexible bodies similar to the rigid systems contain unknown Lagrange multipliers. Therefore, it is necessary to combine the acceleration constraint of flexible body to generate a set of closed mathematical differential equations refer to Eq. (4):

$$M\ddot{q} + \phi_q^T \lambda = g + s - K_{ff}, \tag{3}$$

$$\ddot{\phi} = \phi_q \ddot{q} - \gamma = 0, \tag{4}$$

where: s is quadratic term matrix of absolute angular velocity, g is external force, K_{ff} is stiffness matrix of flexible body.

The rigid-flexible coupling Eq. (8) can be obtained by assembled the rigid body and the flexible body refer to Eq. (5), Eq. (6) and Eq. (7):

$$\ddot{q} = \begin{bmatrix} \vdots \\ \ddot{\gamma}_j \\ \dot{\omega}_j \\ \ddot{w}_i \\ \vdots \end{bmatrix}, \tag{5}$$

$$Q = \begin{bmatrix} \vdots \\ \hat{f}_{rj} \\ \hat{f}_{pj} \\ g_{ri} + s_{ri} \\ g_{pi} + s_{pi} \\ g_{wi} + s_{wi} - K \\ \gamma \\ \vdots \end{bmatrix}, \tag{6}$$

$$Z = \begin{bmatrix} \vdots & & & & & \\ & M_j & & & & \\ & & J_j & & & \\ & & & m_{dd} & m_{dr} & m_{df} \\ & & & m_{dr} & m_{rr} & m_{rf} \\ & & & m_{df} & m_{rf} & m_{ff} \\ & & & & & \vdots \end{bmatrix}. \tag{7}$$

The rigid-flexible coupling pantograph dynamic model Eq. (8) is composed of constraint equations and dynamic equations:

$$\begin{bmatrix} Z & \phi_q^T \\ \phi_q & 0 \end{bmatrix} = \begin{bmatrix} \ddot{q} \\ \lambda \end{bmatrix} = \begin{bmatrix} Q_F + Q_V + K_q \\ \gamma \end{bmatrix}, \tag{8}$$

here: Q_F is external force matrix, Q_V is quadratic matrix of velocity, K_q is flexible deformation matrix.

The pantograph of Chongqing straddle-type monorail line 3 is shown in Fig. 3. The dynamic model of rigid-flexible coupling pantograph is also shown in Fig. 3. Pantograph base, pantograph head base and strip base are rigid bodies. Support rod, lower frame, upper frame and steady rod are flexible bodies. The parameters of monorail pantograph are illustrated in Table 1.

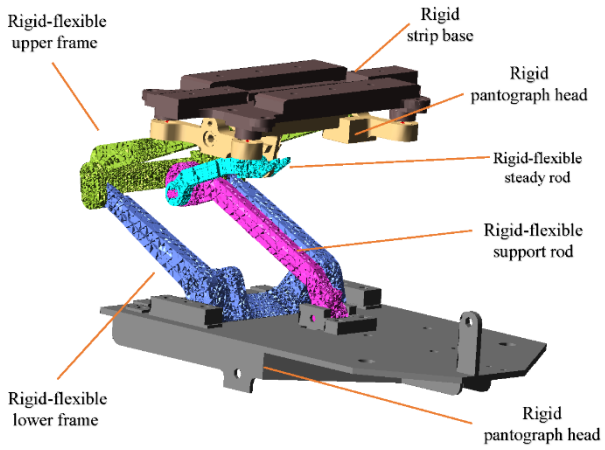

Fig. 3 Rigid-flexible coupling pantograph model

Table 1

Parameters of pantograph

Item	Mate-rial	Mass, kg	*Ixx*, kg.m^2	*Iyy*, kg.m^2	*Izz*, kg.m^2
Head base	Al	0.519	0.0051	0.0042	0.0042
Copper base strip	Cu	0.831	0.0027	0.0026	0.00012
Strip base	Al	1.68	0.014	0.017	0.0035
Upper frame	Al	0.732	0.0021	0.0043	0.0052
Steady rod	Al	0.087	0.000007	0.00016	0.00017
Lower frame	Al	0.151	0.005	0.010	0.014
Supporting rod	Al	0.237	0.000047	0.0020	0.0020

2.2. Dynamic model of catenary

The straddle monorail catenary is composed of insulator, aluminum profiles, contact wire, etc. The catenary of monorail is shown in Fig. 4.

In order to establish the finite element calculation model of catenary, the catenary is discretized into several plane beam elements, and the insulator is replaced by transverse spring. The finite element calculation model of catenary is shown in Fig 5.

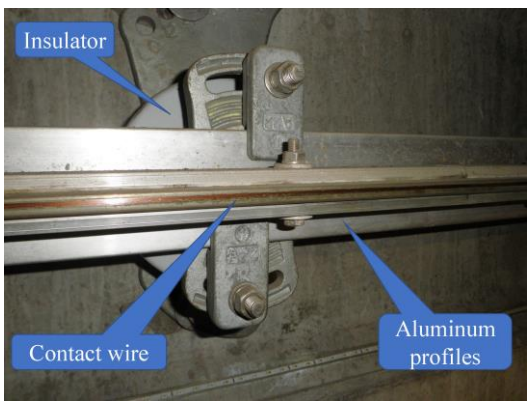

Fig. 4 Catenary of monorail

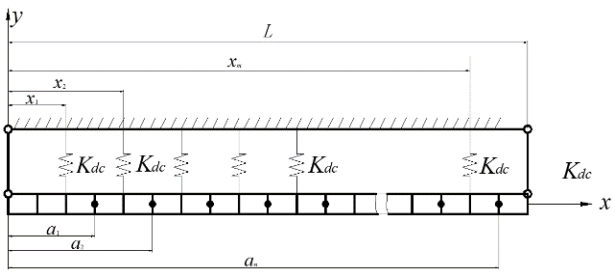

Fig. 5 Finite element dynamic model of rigid catenary

Simply take any plane beam element as the analysis object as shown in Fig. 6. The element has two nodes *i* and *j*. The length of the element is *l*, density is ρ, elastic modulus is *E*, lateral displacement is $V_{(t)}$, rotation angle is $\theta_{(t)}$, transverse force is $F_{y(t)}$, and the bending moment is $M_{(t)}$.

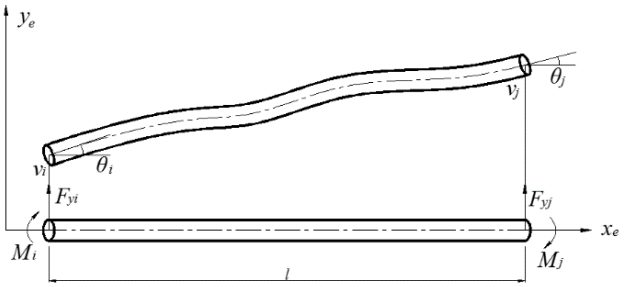

Fig. 6 Plane beam element

The nodal force acting on the element node is F_e; the displacement of the element is Y_e. Eq. (9) is the relationship between nodal force and displacement of beam element:

$$F_e = K_e Y_e = \left[F_{yi}\ M_i\ F_{yj}\ M_j\right]^T \left[v_i\ \theta_i\ v_j\ \theta_j\right]^T . \tag{9}$$

Eq. (10) is the elastic potential energy of beam element:

$$\begin{cases} U^e = \dfrac{1}{2}\iiint \varepsilon_x \sigma_x d_x d_y d_z = \\ \quad = \dfrac{1}{2}\iiint Ey^2 Y_e^T X_e \ddot{X}_e^T B d_V = \\ \quad = \dfrac{1}{2} Y_e^T \left(\int EIB^T X_e \ddot{X}_e^T B d_x\right) Y_e \\ I = \iint y^2 d_y d_z \end{cases} . \tag{10}$$

Eq. (11) is the stiffness matrix of the beam element:

$$\begin{aligned} K_e &= EI\int_0^l B^T X_e \ddot{X}_e^T B d_x = \\ &= EI\int_0^l \left(\frac{\partial N_e}{\partial x^2}\right)^T \left(\frac{\partial N_e}{\partial x^2}\right) d_x . \end{aligned} \tag{11}$$

Eq. (12) is the kinetic energy of the beam element:

$$T^e = \frac{1}{2} Y_e^T M_e Y_e . \tag{12}$$

Eq. (13) is the mass matrix of plane beam element:

$$\begin{aligned} M_e &= \int_0^l \rho S B^T Y_e^T X_e \ddot{X}_e^T B d_x = \\ &= \int_0^l \rho S N_e^T N_e d_x . \end{aligned} \tag{13}$$

Based on Lagrange equation, the dynamic equation of plane beam element is established refer to Eq. (14). The

relationship between local coordinate system and global coordinate system of beam element node displacement refer to Eq. (15). T is the transformation matrix.

Through the coordinate transformation matrix, the stiffness matrix K_e, mass matrix M_e, damping matrix C_e and load matrix F_e of the beam element in the local coordinate system are transformed into the stiffness matrix $\overline{K}_e$, mass matrix $\overline{M}_e$, damping matrix $\overline{C}_e$ and load matrix $\overline{F}_e$ of the beam element in the global coordinate system refer to Eq. (16). Eq. (17) is the dynamic equation of plane beam element in global coordinate system, α is the attitude angle in the local coordinate system:

$$M_e\ddot{Y}_e + C_e\dot{Y}_e + K_eY_e = F_e, \tag{14}$$

$$Y_e = TY_e' = \begin{bmatrix} \cos\alpha & \sin\alpha & 0 & & & \\ -\sin\alpha & \cos\alpha & 0 & & & \\ 0 & 0 & 1 & & & \\ & & & \cos\alpha & \sin\alpha & 0 \\ & & & -\sin\alpha & \cos\alpha & 0 \\ & & & 0 & 0 & 1 \end{bmatrix} Y_e', \tag{15}$$

$$\begin{cases} \overline{K}_e = T^T K_e T \\ \overline{C}_e = T^T C_e T \\ \overline{M}_e = T^T M_e T \\ \overline{F}_e = T^T F_e \end{cases}, \tag{16}$$

$$\overline{M}_e\ddot{Y}_e' + \overline{C}_e\dot{Y}_e' + \overline{K}_eY_e' = \overline{F}_e. \tag{17}$$

The finite element dynamic equation of rigid catenary can be obtained by assembled $\overline{K}_e$, $\overline{M}_e$, $\overline{C}_e$, $\overline{F}_e$ according to order of the node. Eq. (18) is the finite element dynamic equation of rigid catenary. *K*, *M*, *C* and *F*are the stiffness matrix, mass matrix, damping matrix and load matrix in the global coordinate system respectively:

$$M\ddot{Y} + C\dot{Y} + KY = F. \tag{18}$$

2.3. Tire model

Tire models mainly include analytical model, empirical model and semi-empirical tire model. The UA pure analytical tire mechanics model which was developed by the University of Arizona in the United States is used to simulate the running tire, guiding tire and stabilizing tire. UA model can realistically simulate the dynamic interaction force between wheel and track beam, which can accurately reflect the vibration which caused by the irregularity of track. The coordinate system of UA model is shown in Fig 7.

UA pure analytical tire mechanics model simplifies tire into a series of annular three-dimensional springs along radial direction. In the rolling process of tire, the contact dynamic equation between tire and road surface is established according to the spring deformation and the longitudinal, lateral and normal forces between tire and contact surface. The vertical deformation of running tire is shown in Fig. 8.The tire longitudinal force, lateral force, vertical force and aligning moment are solved according to the contact force equation.

Eq. (19) is the vertical deformation of tire:

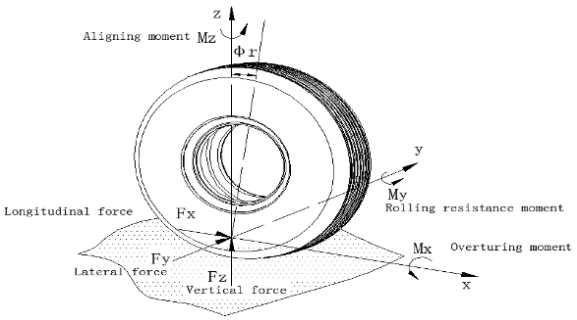

Fig. 7 Coordinate system of UA model

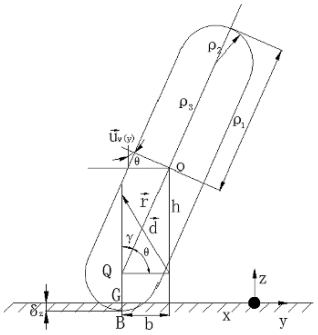

Fig. 8 Vertical deformation of running tire

$$\delta = \vec{r}^{\,G}(z) - \vec{r}^{\,B}(z). \tag{19}$$

Eq. (20) is the vertical force of the tire:

$$F_z = K_z \cdot \delta_z. \tag{20}$$

Eq. (21) is the longitudinal force of the tire:

$$F_x = K_s S_s l_n^2 + \mu_x F_z\left(1 - 3l_n^2 + 2l_n^3\right), \tag{21}$$

$$l_n = \frac{l_a}{l}. \tag{22}$$

Eq. (23) is the lateral force of the tire:

$$F_y = K_\alpha S_\alpha l_n^2 + \mu_y F_z(1 - 3l_n^2 + 2l_n^3) + K_\gamma S_\gamma. \tag{23}$$

Eq. (24) is the aligning moment of the tire:

$$M_z = M_{z1} + M_{z2}, \tag{24}$$

$$\begin{aligned} M_{z1} &= \int_0^l x \cdot \sigma_{y2} \cdot \omega \cdot dx \\ &= \int_0^{la} x \cdot \sigma_{y2}^{(\alpha)} \cdot \omega \cdot dx + \int_{la}^{l} x \cdot \sigma_{y2}^{(s)} \cdot \omega \cdot dx \\ &= \frac{2}{3} K_\alpha S_\alpha l \cdot l_n^3 + \frac{1}{2}\mu_y F_z \cdot l \cdot \left(1 - 4l_n^3 + 3l_n^4\right), \end{aligned} \tag{25}$$

$$\begin{aligned} M_{z2} &= -\frac{1}{2} l F_{y\alpha} = \\ &= -\frac{1}{2} K_\alpha S_\alpha l \cdot l_n^2 - \frac{1}{2}\mu_y F_z \cdot l \cdot \left(1 - 4l_n^2 + 3l_n^3\right), \end{aligned} \tag{26}$$

where: K_z is the vertical stiffness, K_s is the longitudinal slip stiffness, S_s is the longitudinal slip ratio, K_α is the lateral

stiffness, S_α is the lateral slip ratio due to slip angle, u_x is longitudinal friction coefficient, u_y is lateral friction coefficient, β is the directional angle of slip velocity, l_α is the length of adhesion length, l is contact path length, ω is the width of contact patch, K_y is the lateral stiffness, S_y is the lateral slip ratio due to camber angle.

2.4 Track beam model

The track beam of monorail is made of pre-stressed concrete, so the ISO8608 vehicle road standard model is adopted for the track beam roughness model of straddle monorail. The track beam surface power spectral density PSD refer to Eq. (27):

$$G_d(\Omega) = \frac{\alpha}{\Omega^n + \beta^n} = G_d(\Omega_0)\left(\frac{\Omega_0}{\Omega}\right)^{-n}, \quad (27)$$

where: Ω is the spatial frequency (sub/m), α is road surface roughness, β is shape coefficient, n is PSD index coefficient. α, β, and n are obtained by power spectrum fitting and are shown in Table 2.

Table 2

Parameter for track beam model

Parameter	Running surface	Guiding surface	Stabilizing surface
α	0.0004	0.0007	0.0007
β	0.31	0.61	0.5
n	3.1	2.9	2.7

2.5. Rigid-flexible pantograph-catenary-car model

The main parameters of Chongqing straddle-type monorail line 3 are shown in Table 3. The Rigid-flexible coupling pantograph-catenary-car dynamic model is shown in Fig. 9.

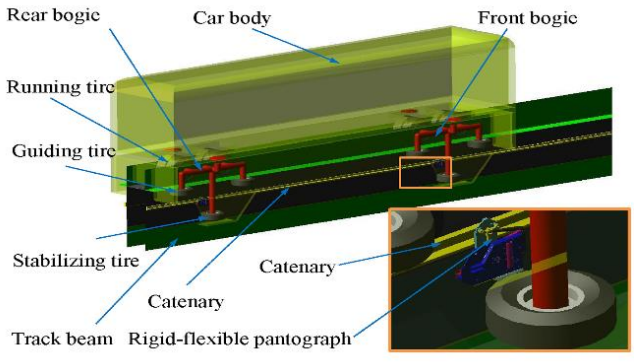

Fig. 9 Rigid-flexible coupling pantograph-catenary-car dynamic model

3. Verification of rigid- flexible pantograph-catenary-car model

Accurate dynamic model is the basis of research of the dynamic performance of pantograph-catenary-car for straddle-type monorail. Therefore, the results of the test and simulation are compared. The process of verification of rigid-flexible coupling pantograph-catenary-car dynamic model is shown in Fig. 10.

Table 3

Main parameters of the monorail

Item	Value	Unit
Width of car body	2980	mm
Length of head car	15500	mm
Length of middle car	14600	mm
Mass of head car	28.6	mm
Mass of middle car	27.6	mm
Axle load	11000	kg
Distance of two bogies	9600	mm
Axle distance of running wheel	1500	mm
Axle distance of guide wheel	2500	mm
Diameter of running wheel	1006	mm
Diameter of guide wheel	730	mm
Diameter of stable wheel	730	mm

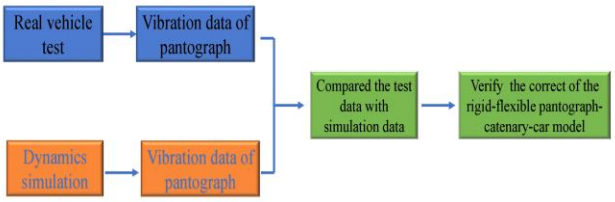

Fig. 10 Verification of rigid-flexible coupling pantograph catenary-car dynamic model

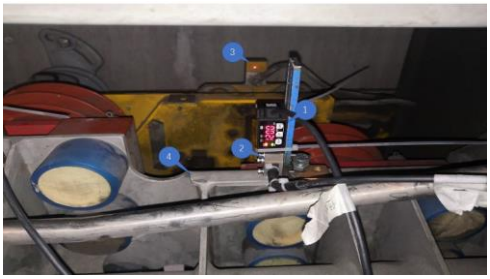

a

b

Fig. 11 Real vehicle test in straddle-type monorail line 3 of Chongqing: a – test progress, b – the instrument of the sensors; *1* - laser displacement sensor, *2* - acceleration sensor, *3* - pantograph head, *4* - mounting seat of pantograph, *5* - computer, *6* - IMC device

The real vehicle test was performed from Huixing station to Changfu road station, in straddle-type monorail line 3 of Chongqing. The pantograph-catenary system adopts DC 1500 V. In order to ensure the safety of the test, the non-contact measurement method is adopted to measure

the displacement of the pantograph head by laser displacement sensor. The vibration of the pantograph installation base is measured by acceleration sensor, and the displacement of pantograph head is measured by laser displacement sensor. The instrument of the test sensors is shown in Fig. 11.

The vibration and displacement of the test results are compared with the simulation in order to verify the correctness of the dynamic model. The simulation and tested results are showed in Fig. 12.

Fig. 12, a shows the comparison of the transverse vibration acceleration from simulated and test in the pantograph installation base when the running speed is 30 km/h. As shown in Fig. 12, a, the frequency response of transverse vibration acceleration spectrum of the simulated is in good agreement with that of the test in the low frequency phase, except for some differences in the amplitude. Fig. 12, b shows the comparison of the pantograph head displacement from simulated and test when the running speed is 30 km/h. As shown in Fig. 12, b, the frequency response of pantograph head displacement spectrum of the simulated is in good agreement with that of the test, except for little differences in the amplitude of the low-frequency phase.

Therefore, it can be concluded that the pantograph-catenary-car dynamic model can accurately simulate the dynamic performance of monorail pantograph-catenary system.

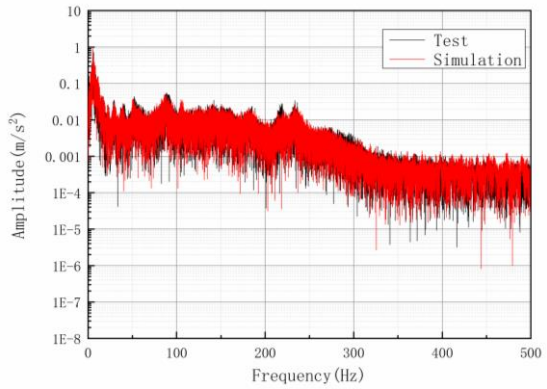

a

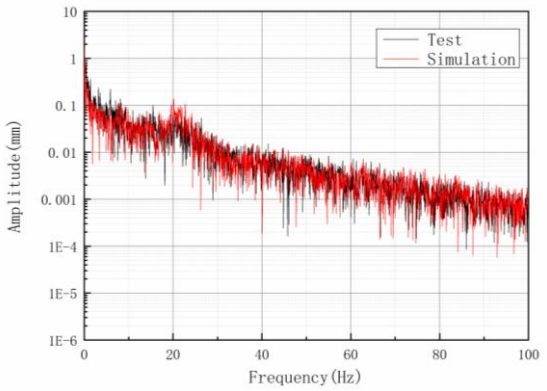

b

Fig. 12 The comparison of test and simulation: a – the comparison of the acceleration of the pantograph installation base, b – the comparison of the pantograph head displacement

4. Results and discussions

The maximum operating speed of straddle monorail vehicle is 80 km/h. In order to evaluate the applicability of the two models, this paper analyzed the contact force response of two model with four different speeds, which are 20 km/h, 40 km/h, 60 km/h and 80 km/h respectively.

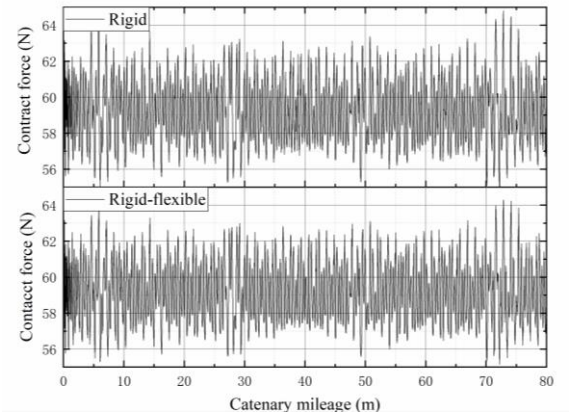

Fig. 13 Contact force at the speed of 20 km/h

Table 4

Current collection quality indexes of contac force at the speed of 20 km/h

Speed, km/h	Model	Mean, N	SD	Max, N	Min, N
20	Rigid	58.68	0.81	61.34	55.87
	Rigid-flexible	58.68	0.72	61.21	56.13

Fig. 13 shows the contact force of pantograph-catenary system at the speed of 20 km/h, Table 4 is the mean value, maximum value, minimum value and standard deviation of contact force. As shown in Table 4, the mean value of contact force of rigid model and rigid-flexible model is 56.68 at the speed of 20 km/h. The standard deviation of contact force of rigid model is 0.81, while the rigid- flexible model is 0.72. The maximum value of contact force of rigid model is higher than rigid-flexible model, and the minimum value of contact force of rigid model is lower than rigid-flexible model.

Fig. 14 shows the contact force of pantograph-catenary system at the speed of 40 km/h, Table 5 presents the mean value, maximum value, minimum value and standard

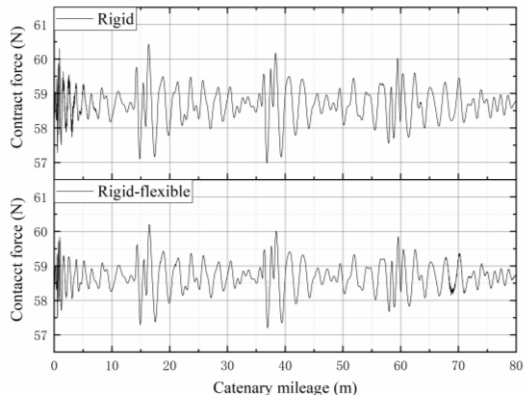

Fig. 14 Contact force at the speed of 40 km/h

Table 5

Current collection quality indexes of contact force at the speed of 40 km/h

Speed, km/h	Model	Mean, N	SD	Max, N	Min, N
40	Rigid	58.69	0.52	60.54	56.98
	Rigid-flexible	58.69	0.45	60.31	57.20

deviation of contact force. As shown in Table 5, the mean value of contact force of rigid model and rigid-flexible model is 58.69 at the speed of 40 km/h. The standard deviation of contact force of rigid model is 0.52, while in the rigid- flexible model, the standard deviation of contact force of is 0.45. The maximum value of contact force of rigid model is higher than rigid-flexible model, and the minimum value of contact force of rigid model is lower than rigid-flexible model.

Fig. 15 shows the contact force of pantograph-catenary system at the speed of 60 km/h, Table 6 is the mean value, maximum value, minimum value and standard deviation of contact force. As shown in Table 6, the mean value of contact force of rigid model and rigid-flexible model is 58.68 at the speed of 60 km/h. The standard deviation of contact force of rigid model is 0.65, while in the rigid- flexible model, the standard deviation of contact force of is 0.55. The maximum value of contact force of rigid model is higher than rigid-flexible model, and the minimum value of contact force of rigid model is lower than rigid-flexible model.

Fig. 16 shows the contact force of pantograph-catenary system at the speed of 80 km/h, Table 7 is the mean value, maximum value, minimum value and standard deviation of contact force. As shown in Table 7, the mean value of contact force of rigid model and rigid-flexible model are 58.68 and 58.69 at the speed of 80 km/h. The standard deviation of contact force of rigid model is 0.51, while in the

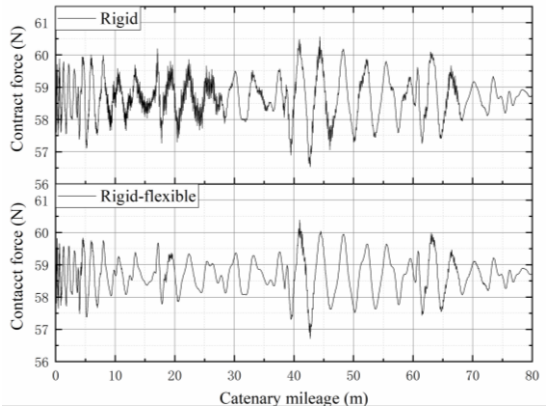

Fig. 15 Contact force at the speed of 60 km/h

Table 6

Current collection quality indexes of contact force at the speed of 60 km/h

Speed, km/h	Model	Mean, N	SD	Max, N	Min, N
60	Rigid	58.68	0.65	60.56	56.53
	Rigid-flexible	58.68	0.55	60.38	56.71

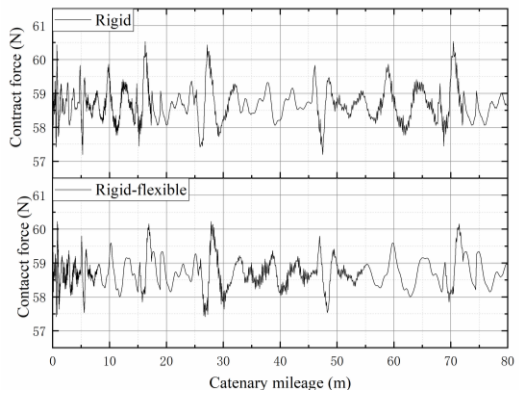

Fig. 16 Contact force at the speed of 80 km/h

rigid-flexible model, the standard deviation of contact force of is 0.45. The maximum value of contact force of rigid model is higher than rigid-flexible model, and the minimum value of contact force of rigid model is lower than rigid-flexible model.

Table 7

Current collection quality indexes of contact force at the speed of 80 km/h

Speed, km/h	Model	Mean, N	SD	Max, N	Min, N
80	Rigid	58.68	0.51	60.53	57.20
	Rigid-flexible	58.69	0.45	60.22	57.41

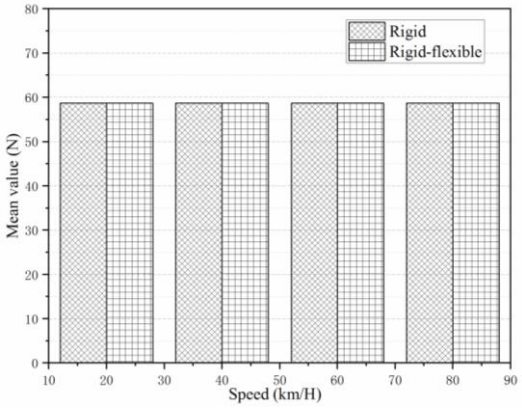

a

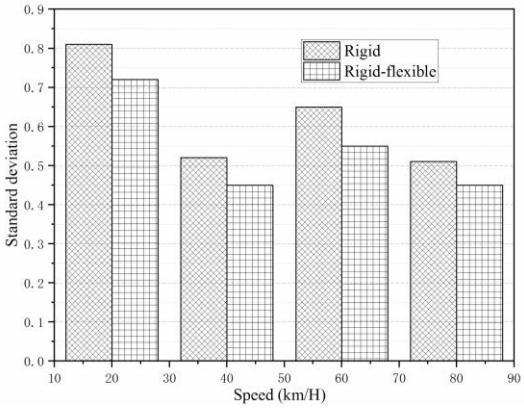

b

Fig. 17 Comparison of the contact force: a – mean value of contact force, b – standard deviation of contact force

It can be seen from Fig. 17, a that the mean value of rigid pantograph model and rigid-flexible pantograph model is almost the same, and the mean value remains unchanged with the increase of running speed. It can be seen from Fig. 17, b that the standard deviation of rigid-flexible pantograph model is smaller than that of rigid pantograph model due to the effects of structure flexibility. Therefore, the rigid-flexible pantograph catenary coupling system has the better current collection quality at the same speed.

The rigid model and rigid-flexible model have the best current collection quality at the running speed of 40 km/h and 80 km/h, and has the worst current collection quality at the at the running speed of 20 km/h.

Figs. 18-21 show the spectrograms of pantograph head lateral vibration accelerations in the range of 0~50 Hz. It shows that the frequency response of pantograph head calculated by the rigid pantograph model are close to that of rigid-flexible pantograph model. However, small difference occurs in the amplitude of the two model in the same frequency.

Fig. 18 shows that the spectrograms of the two models have two obvious peaks at the vehicle running speed of 20 km/h, the frequency of the rigid model is 0.27 Hz and 9.47 Hz, the frequency of the rigid-flexible model is 0.27 Hz and 9.47 Hz. When the frequency is 0.27 Hz, the amplitude of the rigid model is 0.21, the amplitude of the rigid-flexible model is 0.19. When the frequency is 9.47 Hz, the amplitude of the rigid model is 0.11, the amplitude of the rigid-flexible model is 0.11. The vibration amplitude of rigid pantograph

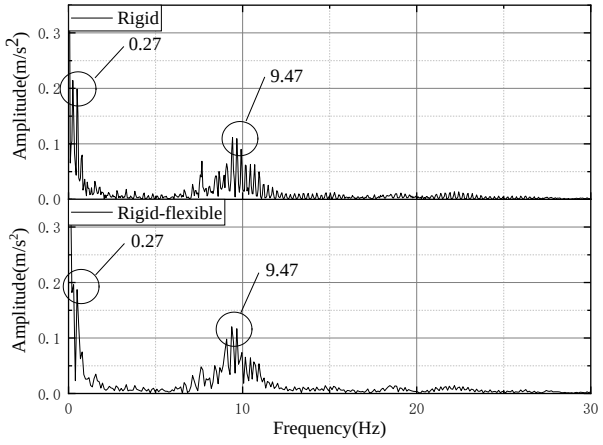

Fig. 18 Frequency spectrum of pantograph head acceleration at the speed of 20 km/h

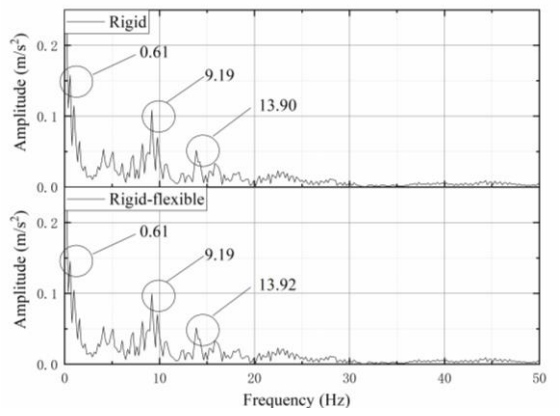

Fig. 19 Frequency spectrum of pantograph head acceleration at the speed of 40 km/h

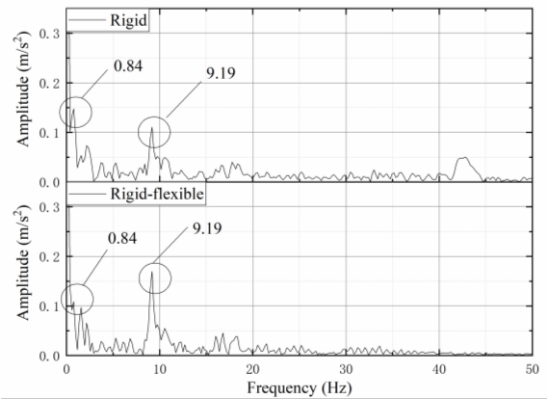

Fig. 20 Frequency spectrum of pantograph head acceleration at the speed of 60 km/h

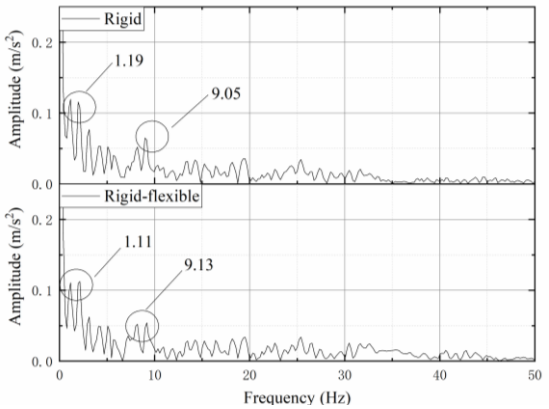

Fig. 21 Frequency spectrum of pantograph head acceleration at the speed of 80 km/h

is slightly larger than that of flexible pantograph at the frequency is 0.27 Hz.

Fig. 19 shows that the spectrograms of the two models have two obvious peaks at the vehicle running speed of 40 km/h, the frequency of the rigid model is 0.61 Hz, 9.19 Hz and 13.90 Hz, the frequency of the rigid-flexible model is 0.61 Hz, 9.19 Hz and 13.92 Hz. When the frequency is 0.27Hz, the amplitude of the rigid model is 0.16, the amplitude of the rigid-flexible model is 0.14. When the frequency is 9.19 Hz, the amplitude of the rigid model is 0.11, the amplitude of the rigid-flexible model is 0.10. When the frequency is about 13.90 Hz, the amplitude of the rigid model is 0.05, the amplitude of the rigid-flexible model is 0.05. The vibration amplitude of rigid pantograph is slightly larger than that of flexible pantograph at the frequency is 0.61 Hz.

Fig. 20 shows that the spectrograms of the two models have two obvious peaks at the vehicle running speed of 60 km/h, the frequency of the rigid model is 0.84 Hz and 9.19 Hz, the frequency of the rigid-flexible model is 0.84 Hz and 9.19 Hz. When the frequency is 0.84 Hz, the amplitude of the rigid model is 0.15, the amplitude of the rigid-flexible model is 0.11. When the frequency is 9.19 Hz, the amplitude of the rigid model is 0.11, the amplitude of the rigid-flexible model is 0.17. The vibration amplitude of rigid pantograph is slightly larger than that of flexible pantograph at the frequency is 0.84 Hz.

Fig. 21 shows that the spectrograms of the two models have two obvious peaks at the vehicle running speed of 80 km/h, the frequency of the rigid model is 1.19 Hz and 9.05 Hz, the frequency of the rigid-flexible model is 1.14 Hz

and 9.20 Hz. When the frequency is about 1.1 Hz, the amplitude of the rigid model is 0.12, the amplitude of the rigid-flexible model is 0.11. When the frequency is about 9.2 Hz, the amplitude of the rigid model is 0.06, the amplitude of the rigid-flexible model is 0.05. The vibration amplitude of rigid pantograph is slightly larger than that of flexible pantograph at the frequency is 1.14 Hz.

Based on the results shown in Figs.18-21, the flexibility of the pantograph will not affect the main frequency of the vibration of the pantograph head in pantograph-catenary system. In the low frequency vibration below 2 Hz, the vibration amplitude of rigid pantograph is larger than that of rigid-flexible pantograph. When the frequency is about 9 Hz, the vibration amplitude of rigid pantograph is lower than that of rigid-flexible pantograph at the running speed is 20 km/h and 40 km/h, and the vibration amplitude of rigid pantograph is lower than that of rigid-flexible pantograph at the running speed is 40 km/h and 80 km/h.

The flexibility of pantograph will decrease the vibration amplitude of low frequency vibration below 2 Hz of pantograph head and the standard deviation of rigid-flexible pantograph model is smaller than that of rigid pantograph model due to the effects of structure flexibility. Therefore, the low-frequency vibration below 2 Hz of pantograph catenary system will affect the current collection quality of pantograph system.

5. Conclusions

A rigid-flexible pantograph-catenary coupling dynamics model which consider the random irregularity of track beam is proposed to study the effects of pantograph flexibility on the dynamics performance of pantograph-catenary system in straddle-type monorail. In order to verify the accurate of the model, the results of the test and simulation are compared. The simulation results are consistent with the test and the conclusions are as follows:

1. The vibration amplitude of low-frequency vibration below 2 Hz of pantograph catenary system will affect the vibration characteristics and of pantograph-catenary system. The current collection quality of pantograph-catenary system can be improved by reducing the amplitude of low frequency vibration.

2. The pantograph-catenary system has the best current collection quality at the running speed of 40 km/h and 80 km/h, and has the worst current collection quality at the at the running speed of 20 km/h. During operation of monorail, the speed of 20 km/h shall be avoided.

Acknowledgements

Fund Project: Chongqing Key Laboratory of urban rail transit system integration and control. Project Name: Analysis of dynamic characteristics of monorail pantograph and its influence on current collection quality. Project Number: CKLURTSIC-KFKT-212002.

Fund Project: Scientific and Technological Research Program of Chongqing Municipal Education commission. Project Name: Research on the off-line mechanism and wear reducing countermeasures of straddle-type monorail pantograph considering three-dimensional excitation of track beams. Analysis of dynamic characteristics of monorail pantograph and its influence on current collection quality. Project Number: KJQN 202200742.

References

1. **Timan, P. E.** 2015. Why Monorail Systems Provide a Great Solution for Metropolitan Areas, Urban Rail Transit 1: 13-25. http://dx.doi.org/10.1007/s40864-015-0001-1.
2. **Du, Z.; Zhou, J.; Yang, Z.; Bo, J.** 2018. The research on operational reliability evaluation of straddle-type monorail vehicle, Systems Science & Control Engineering 6(1): 537-546. https://doi.org/10.1080/21642583.2018.1550690.
3. **Goda, K.; Nishigaito, T.; Hiraishi, M.; Iwasaki, K.** 1999. Response Analysis caused by Track Irregularity for a Monorail Car: A Study for Dynamic Model Considering the Direction of Tire Force, Transactions of the Japan Society of Mechanical Engineers Series C 65(637): 3546-3552. http://dx.doi.org/ 10.1299/kikaic.65.3546.
4. **He, X.** 2015. Application and Prospect of Straddle Monorail Transit System in China, Urban Rail Transit 1: 26-34. http://dx.doi.org/10.1007/s40864-015-0006-9.
5. **Song, Y.; Liu, Z.; Rønnquist, A.; Navik, P., Liu, Z.** 2020. Contact Wire Irregularity Stochastics and Effect on High-speed Railway Pantograph-Catenary Interactions, IEEE Transactions on Instrumentation and Measurement 69(10): 8196-8206. https://doi.org/10.1109/TIM.2020.2987457.
6. **Song, Y.; Liu, Z.; Lu, X.** 2020. Dynamic Performance of High-speed Railway Overhead Contact Line Interacting with Pantograph Considering Local Dropper Defect, IEEE Transactions on Vehicular Technology 69(6): 5958-5967. https://doi.org/10.1109/TVT.2020.2984060.
7. **Pombo, J.; Ambrósio, J.** 2013. Environmental and track perturbations on multiple pantograph interaction with catenaries in high-speed trains, Computers & Structures 124: 88-101. http://dx.doi.org/10.1016/j.compstruc.2013.01.015.
8. **Massat, J. P.; Laurent, C.; Bianchi, J. P.; Balmès, E.** 2014. Pantograph catenary dynamic optimisation based on advanced multibody and finite element co-simulation tools, Vehicle System Dynamics 52 (sup1): 338-354. http://dx.doi.org/10.1080/00423114.2014.898780.
9. **Shimanovsky, A.; Yakubovich, V.; Kapliuk, I.** 2016. Modeling of the pantograph-catenary wire contact interaction, Procedia Engineering 134: 284-290. http://dx.doi.org/10.1016/j.proeng.2016.01.009.
10. **Ambrósio, J.; Rauter, F.; Pombo, J.; Pereira, M. S.** 2011. A Flexible Multibody Pantograph Model for the Analysis of the Catenary–Pantograph Contact. In: Arczewski, K., Blajer, W., Fraczek, J., Wojtyra, M. (eds) Multibody Dynamics. Computational Methods in Applied Sciences, vol 23. Springer, Dordrecht. http://dx.doi.org/10.1007/978-90-481-9971-6_1.
11. **Zhang, W.; Liu, Y.; Mei, G.** 2006. Evaluation of the coupled dynamical response of a pantograph-catenary system: contact force and stresses, Vehicle System Dynamics 44(8): 645–658. http://dx.doi.org/10.1080/00423110600744656.
12. **Cho, Y. H.** 2008. Numerical simulation of the dynamic

responses of railway overhead contact lines to a moving pantograph, considering a nonlinear dropper, Journal of Sound and Vibration 315(3): 433–454. http://dx.doi.org/10.1016/j.jsv.2008.02.024.
13. **Schaub, M.; Simeon, B.** 2001. Pantograph-Catenary Dynamics: An Analysis of Models and Simulation Techniques, Mathematical and Computer Modelling of Dynamical Systems 7(2): 225-238. http://dx.doi.org/10.1076/mcmd.7.2.225.3644.
14. **Wang, H.; Liu, Z.; Song, Y.; Lu, X.; Han, Z.; Zhang, J.; Wang, Y**. 2016. Detection of Contact Wire Irregularities Using a Quadratic Time-Frequency Representation of the Pantograph-Catenary Contact Force, IEEE Transactions on Instrumentation and Measurement 65(6): 1385-1397. https://doi.org/10.1109/TIM.2016.2518879.
15. **Flores, P.; Machado, M.; Silva, M. T.; Martins, J. M.** 2010. On the continuous contact force models for soft materials in multibody dynamics, Multibody System Dynamics 25(3): 357-375. http://dx.doi.org/10.1007/s11044-010-9237-4.
16. **Lee, K.** 2011. A short note for numerical analysis of dynamic contact considering impact and a very stiff spring-damper constraint on the contact point, Multibody System Dynamics 26: 425–439. https://doi.org/10.1007/s11044-011-9257-8.
17. **Pereira; C. M.; Ramalho, A. L.; Ambrósio, J. A.** 2010. A critical overview of internal and external cylinder contact force models, Nonlinear Dynamics 63(4): 681-697. https://doi.org/10.1007/s11071-010-9830-3.
18. **Xu, Z.; Song, Y.; Liu, Z.** 2020. Effective Measures to Improve Current Collection Quality for Double Pantographs and Catenary Based on Wave Propagation Analysis, IEEE Transactions on Vehicular Technology 69(6): 6299-6309. http://dx.doi.org/10.1109/TVT.2020.2985382.
19. **Lee, J. H.; Kim, Y. G.; Paik, J. S.; Park, T. W.** 2012. Performance evaluation and design optimization using differential evolutionary algorithm of the pantograph for the high-speed train, Journal of Mechanical Science and Technology 26(10): 3253-3260. http://dx.doi.org/10.1007/s12206-012-0833-5.
20. **Benet, J.; Cuartero, N.; Cuartero, F.; Rojo, T.; Tendero, P.; Arias, E.** 2013. An advanced 3D-model for the study and simulation of the pantograph catenary system, Transportation Research Part C: Emerging Technologies 36: 138-156. http://dx.doi.org/10.1016/j.trc.2013.08.004.
21. **Yang, Z.; Du, Z.; Chen, C.; Wen, X.; Xu, Z.** 2017. Research on the Influence of Straddle-Type Monorail's Pantograph Head Parameter on Power Collection Quality, Urban Rail Transit (3): 149-157. http://dx.doi.org/10.1007/s40864-017-0066-0.
22. **Luo, L.; Jianghua, T.** 2009. Improving Interaction between Pantographs and Catenaries of Chongqing Monorail System, Urban Rapid Rail Transit (4): 80-82.

Z. Yang, Z. Du, Z. Xu, L. Xin, Z. Huo

PANTOGRAPH-CATENARY COUPLING SYSTEM DYNAMICS WITH RIGID-FLEXIBLE PANTOGRAPH FOR STRADDLE-TYPPE MONORAIL

S u m m a r y

The flexible pantograph of straddle-type monorail has influence on the dynamics performance of pantograph-catenary system. This paper established a rigid-flexible pantograph-catenary-vehicle coupling dynamics model of monorail. By embedded the rigid-flexible pantograph into the vehicle dynamic analysis model, the rigid-flexible pantograph-catenary coupling dynamics model that could consider the random irregularity of track beam ultimately established. The validity of model has been approved by the pantograph dynamics test of Chongqing monorail line 3. The dynamic performance of the pantograph-catenary system, calculated by the dynamics models with rigid and rigid-flexible pantograph are compared in detail. The results show that the pantograph flexibility affects the vibration characteristics and the current collection quality of pantograph-catenary system.

Keywords: straddle-type monorail, rigid-flexible pantograph-catenary, multibody dynamics.

Received August 28, 2023
Accepted August 19, 2024